# Effect of different pitch angles on the performance parameter of the horizontal axis wind turbine using computational fluid dynamics

RAJENDRA ROUL[1] and AWADHESH KUMAR[1]

[1]National Institute of Technology Rourkela

May 5, 2020

**Abstract**

Wind energy is one of the clean, sustainable types of energy that can deal with the current worldwide non-renewable energy source emergency. Even though it adds to 2.5% of the worldwide power request, with depletion of petroleum derivative sources, extraction of wind energy must reach to a more prominent degree to meet the energy emergency and issue of contamination. Now, to improve the aerodynamic response of a wind turbine, the blade pitch control is an effective method, usually applied to large-scale wind turbines. The present work incorporates an investigation of the impact of varied pitch angles on the performance parameters of a horizontal axis wind turbine. CFD code Fluent has been used to perform the simulations. A total of eight pitch angles are considered in this investigation. In addition to it, a numerical investigation of S809 airfoil has been performed and validated by a series of benchmark data. The SST k-w turbulence model has been utilized. The steady-state simulation is performed around a HAWT blade using multiple reference frame. It is seen that torque increases with an increase in wind velocity and decreases with an increase in pitch angle. The optimum pitch angle is obtained for maximum power generation.



# INTRODUCTION

From the past ten years, the usage and supply of fossil fuels are decreasing due to their harmful impact on the environment, which on the other hand, increases the demand for renewable energy sources [1].Support for the usage of renewable energy sources has been increased, not because of the enhancement of power efficiency, but due to maintaining the criteria of climate goals [2] and consequently intensify the dependency of the renewable energy source as a means to mitigate the traditional way to generate energy on the environment. Electricity not only becomes an indispensable factor for the growth and improvement of human society but also plays a vital role in the industrial sector for economic and product development [3].Due to this reason power becomes a source that it should be accessible to every other corner of the world. One way to generate electricity is to use wind as a renewable energy source and utilize it through wind turbine which can convert the kinetic energy present in the wind to meaningful electricity [4]. Another way is the usage of the photovoltaic cell, where electricity production is executed by converting the solar radiation through the process of the photoelectric effect. Despite greater performance and cost-effectiveness of photovoltaic panel technology, the usage of wind energy has reached a greater extent in the last few years. For instance, in 2017, 34% of the increase in wind power installation has been observed in Europe as compared to 2016[5]. Due to an increase in demand, wind turbine technology has become a prominent area for doing research. Various control techniques have been executed to enhance the power output and control the structural damage due to aeroelasticity. Apart from this, various research has been focused on intensifying the use of wind turbines in a turbulence environment. Bahaj et al. proposed that, as an alternative to traditional energy supply, micro-generation technology is also providing power to the user's home or buildings [6].Miller et al. [7] analyses different numerical techniques implemented in the wind energy industry which incorporate the

significant territories for research, such as micro-scale siting, wind modeling and forecast, blade optimization, flow modeling and support structure investigation. The prediction of blade aerodynamics is required for the performance of the turbine, and two significant strategies for numerical prediction has been considered, and they are blade element momentum theory and computational fluid dynamics. A few investigations that have been done by utilizing these strategies for the prediction of turbine performance are incorporated as follows: Lanzafame and Messina [8] used the code based on BEM and utilized it to operate HAWT to its maximum power coefficients. They observed that there is an optimum rotational velocity which gives maximum power for a given streamline velocity. The dynamic stall model has been implemented in modified BEM theory by Dai et al. [9] to predict the forces on large scale wind turbines. It was inferred that this dynamic model is best suited for engineering purposes. Vaz et al. [10] utilizes BEM and develop a mathematical model for the design of a horizontal axis wind turbine blade. Various researchers have used the CFD technique to simulate the NREL turbines by solving Navier stokes equations. As CFD is capable of simulating the complete flow field, the results obtained from these methods are more accurate than the BEM method. CFD simulation of the NREL phase II turbine has been done by Duque et al. [11], and both NREL phase II and NREL phase III turbines simulation is executed by Xu and Sankar [12]. However, the numerical investigation of NREL phase VI turbine using CFD is simulated by Xu and Sankar [13], Johansen et al. [14], Duque et al. [15] and Sezer-Uzol and Long [16].Thumthae and Chitsomboon [17] used the blade of no twist for getting the optimal angle of attack for different wind speed by performing the numerical simulation. The operating conditions considered for this simulation includes pitch angles 1°, 3°, 50, 7° and 12° for the wind speed of 7.2, 8.0, 9.0 and 10.5 m/s. The results obtained from CFD Analysis were validated against the NREL experimental results. Mo and Lee [18] investigated small-sized wind turbines of NREL phase VI to understand its aerodynamic behavior by using the CFD technique, and they considered five different wind velocity in the range of 7 m/s and 25 m/s with a global pitch angle of 5°. SST k-w model was considered for turbulence modeling. They observed stall near the root of the blade at 7 m/s. Li et al. [19] use incompressible dynamic overset code CFD ShipIowa v4.5 to carry out the numerical investigation on the performance full-scale NREL phase VI turbine. The study was accomplished by fixing the pitch angle of blade as 3° and varying the wind velocities to 5. 10. 15 and 25 m/s, and changing the pitch angles from 15° to 40° at a fixed wind speed of 15 m/s. simulation was completed by taking the rotational speed of 72 rpm and using turbulence model as detached eddy simulation. Various performance parameters like power, thrust and pressure variation around airfoil were validated with the experimental results. In this way, it is seen that the pitch angle has an impact on the turbine performance, and for maximum power, it is necessary to observe the best pitch angle for given wind speed and rotor speed. The target of the present work is to analyze the impact of a pitch angle on the performance and aerodynamics of a horizontal axis wind turbine, NREL Phase VI at various wind speeds. In the present investigation, the impact of pitch angle in the horizontal axis wind turbine blade is identified along with the S809 airfoil analysis. This investigation can give data to the researcher to design and optimize the blade effectively by identifying the optimum pitch angle for the corresponding velocity.

This paper is structured as follows. Section 2 presents the governing equations; the next methodology is present in section 3 comprising two components, i.e., wind turbine model, and CFD modeling, Results, and discussions are presented in Section 3, followed by a conclusion in Section 4.

# GOVERNING EQUATIONS

In this study, CFD has been used to carry out aerodynamic analysis of a wind turbine blade in which Navier-Stokes equations are used to accomplish the simulations. Navier-stokes equation encompasses three conservation laws; known as the conservation of mass, conservation of energy and conservation of momentum as mentioned in the following[20]

$$\frac{\partial \rho}{\partial t} + \frac{\partial}{\partial x}(\rho \cup) + \frac{\partial}{\partial y}(\rho) + \frac{\partial}{\partial z}(\rho \omega) = 0 (1)$$

$$\rho \frac{\mathrm{Du}}{\mathrm{Dt}} = \frac{\partial(-p+\tau_{\mathrm{xx}})}{\partial x} + \frac{\partial \tau_{\mathrm{yx}}}{\partial y} + \frac{\partial \tau_{\mathrm{zx}}}{\partial z} + S_{\mathrm{Mx}} (2)$$

$$\rho\frac{\mathrm{Dv}}{\mathrm{Dt}} = \frac{\partial\tau_{\mathrm{xy}}}{\partial x} + \frac{\partial(-p+\tau_{\mathrm{yy}})}{\partial y} + \frac{\partial\tau_{\mathrm{zy}}}{\partial z} + S_{\mathrm{My}} \quad (3)$$

$$\rho\frac{\mathrm{Dw}}{\mathrm{Dt}} = \frac{\partial\tau_{\mathrm{xz}}}{\partial x} + \frac{\partial\tau_{\mathrm{yz}}}{\partial y} + \frac{\partial(-p+\tau_{\mathrm{zz}})}{\partial z} + S_{\mathrm{Mz}} \quad (4)$$

Where

u, v and w =components of the velocity in the x, y and z-direction respectively.

P = pressure

$\tau_{\mathrm{ij}}$ = the normal and shear stress that affects the 3D fluid particles.

$S_{\mathrm{Mx}}, S_{\mathrm{My}}, and\ S_{\mathrm{Mz}}$ = Body forces per unit of mass in the x, y, and z-direction.

# METHODOLOGY

## Wind turbine model

The wind turbine model used in this study is the NREL PHASE VI wind turbine [21]. It is a wind turbine designed by NREL (National Renewable Energy Laboratory). It uses S809 airfoil from root to tip.it is also twisted along the span. The cross-sections of airfoil along the blade length which is accompanied by chord and twist distributions, are shown in Figure 1 and figure 2. The 3d geometry model is established using Ansys Fluent [22] is presented in figure 3 and the corresponding airfoil is shown in figure 4.Technical parameters of the blade is shown in table 1

Table 1 main parameters of NREL PHASE VI Wind turbine

| Parameters | Values | units |
|---|---|---|
| Rated power $\mathrm{P_{rated}}$ | 19.8 | KW |
| Number of blades | 2 | NA |
| Rotor radius | 5.532 | m |
| Hub height | 12.192 | m |
| Cut in speed | 6 | m/s |
| Cut out speed | 72 | rpm |

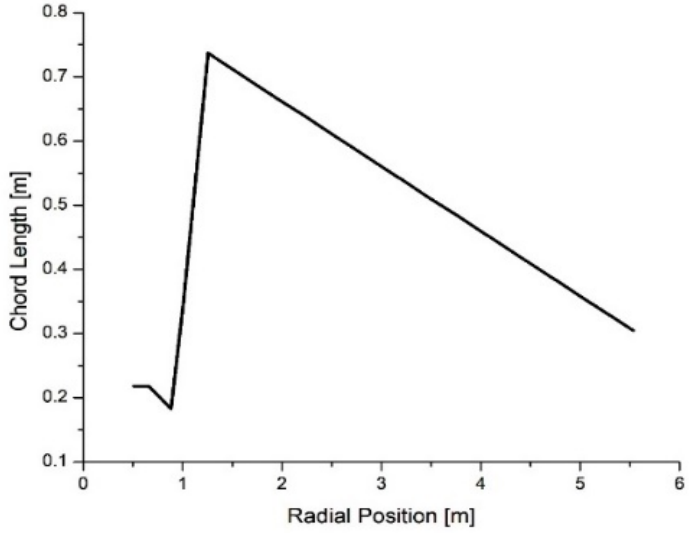


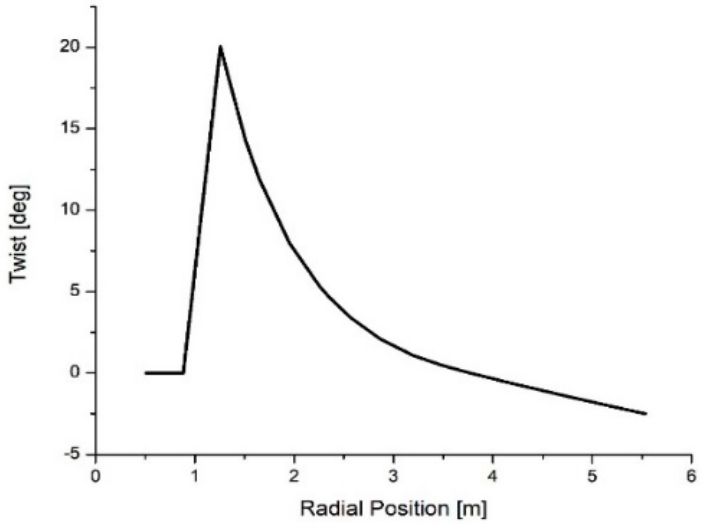

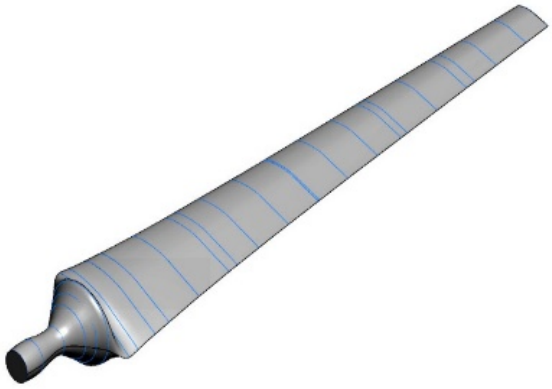

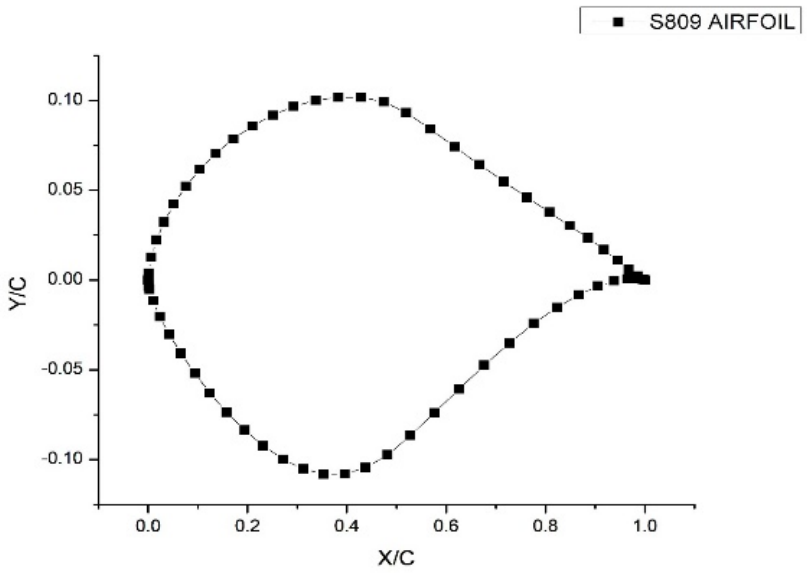


## CFD MODELLING

ANSYS FLUENT has been used to establish a CFD model, which is a software used for CFD modeling. In this section, CFD modeling of NREL PHASE VI wind turbine blades has been performed. The computational domain and boundary conditions, mesh, turbulence model, solution method and convergence criteria used in the CFD modeling are presented in this section

**Computational domain of airfoil, blade and their boundary conditions**

The use of Ansys commercial software performs the construction of the computational domain and grid generation for S809 airfoil. It is widely accepted that the use of the C-shaped domain is quite dominated in 2D airfoil simulations [23-26]. So, the designed C-Shaped Domain, along with S809 airfoil and boundary conditions, are presented in figure 5.

From the previous work, it has been found that NREL PHASE VI is a two-blade turbine and it possesses $180^0$ periodicity and hence one blade is modeled while performing CFD analysis. However, in this study author is trying to investigate the performance of the NREL PHASE VI turbine by considering three blades., Due to the symmetric nature of a three-blade wind turbine, the domain is made for a single blade to reduce computational time and by using periodicity, the solution of flow simulation around one blade gets extrapolated to two other blades to visualize the complete rotor [27-29]. The domain follows the 120° radial stream tube design in which the velocity inlet is kept behind 12 m from the blade and maintained the arc of 12 m radius. Whereas, the pressure outlet is placed at 24 m from the blade and the outlet surface maintained the arc of 24 m radius. The top surface is also considered to be the inlet and exhibit the same velocity. The computational domain and boundary conditions for the wind turbine model are depicted in Figure 6.

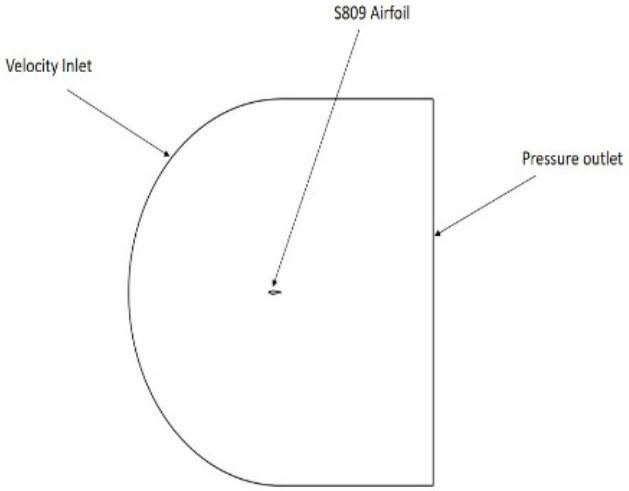

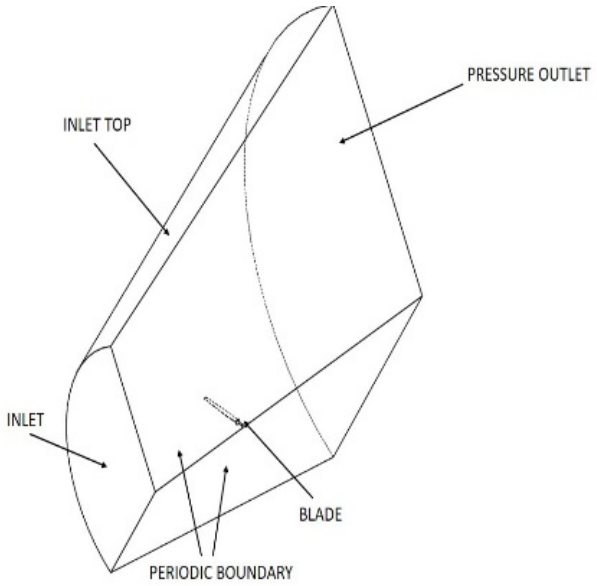


**CFD meshing of airfoil and blade**

The meshing of the C-shaped domain of the airfoil starts with global mesh control by activating advance size function for resolving regions with curvature for determining the Edge and Face sizes based on Curvature Normal Angle. In addition to it, local mesh control is also implemented which contributes mapped face meshing and three edge sizing. First edge sizing highlights the c portion of the domain with 100 number of divisions, second edge and third edge sizing consist of 50 division each with first two bias factor of 150. As illustrated in figure 5, the outer boundary of the computational domain is C-type with radius 12.5 airfoil chord length for better simulating the wake region downstream of the airfoil. The base of the domain is 25 airfoil chord length. The mesh consists of 10251 nodes and 10050 elements. Figure 9 and figure 10 shows the meshing of C- shape domain and close view of airfoil. By using identical boundary and computational conditions, the pressure and velocity distributions were obtained by the software.

For blade, it is meshing start with the same global mesh control followed by local mesh handling. While controlling global mesh, it is ascertained that tetrahedral cells get optimized automatically for CFD and FLUENT. To make the curve with the desired shape and skewness, the advanced size function is changed to proximity and curvature, with relevance center maintained at a medium level. To ensure the good meshing, local mesh inverting these algebraic equations gives the value of (u, v, w, p, k, and $\omega$) at the cell centers. Here, u, v, and w indicate the velocity in x, y and z-direction and, k and w reflect kinetic energy and specific dissipation constant used for turbulence modeling. Here, the fluid domain is generated automatically as tetrahedral shaped which is given in figure 7. Moreover, to capture the boundary layer on an object, the prismatic inflation layer is applied for external flow and is shown in figure 8. To create more refinement around the circumference of the blade surface sphere of influence has been adopted with a radius of 5m and an element size of 2m.

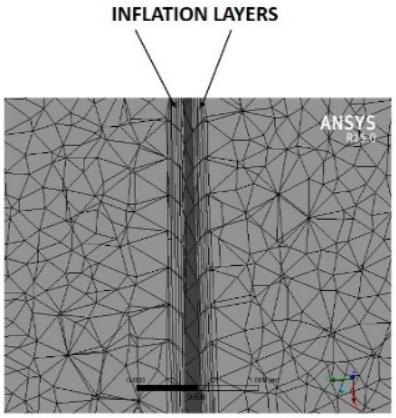


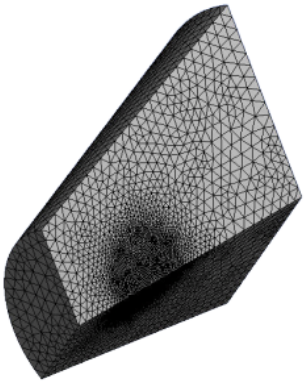

To determine the appropriate cell face size for the blade surfaces, a mesh sensitivity analysis has been conducted. Four cell face size has been taken into consideration, i.e., 0.5m, 0.4m, 0.3m and 0.2m.the associated mesh size, total no of elements and calculated rotor torque is given in table 3 and figure 7. As can be seen from figure 11 and table 2, rotor torque converges at mesh size 0.3m. Further refinement of mesh size to 0.2 only obtain minor difference but it increases the computational time. Considering computational time and accuracy, the mesh size of 0.3 is deemed as an appropriate cell face size at the blade surface for CFD modeling in this study.

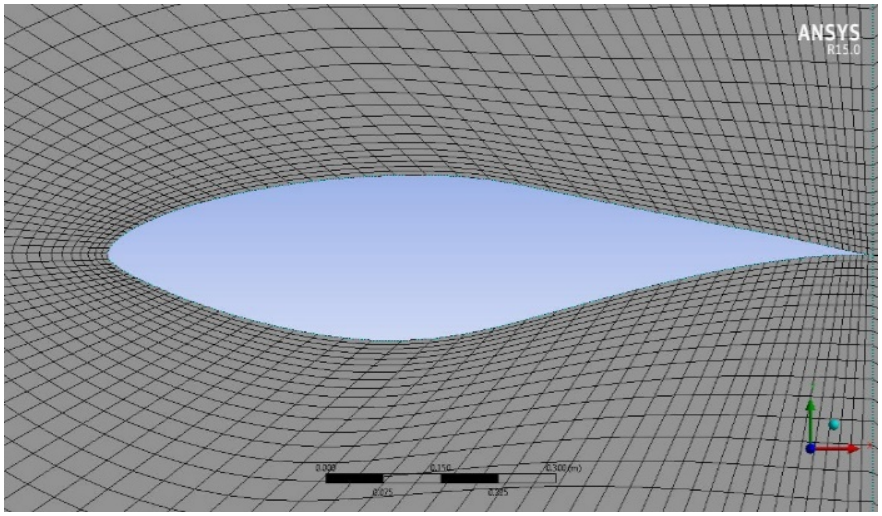


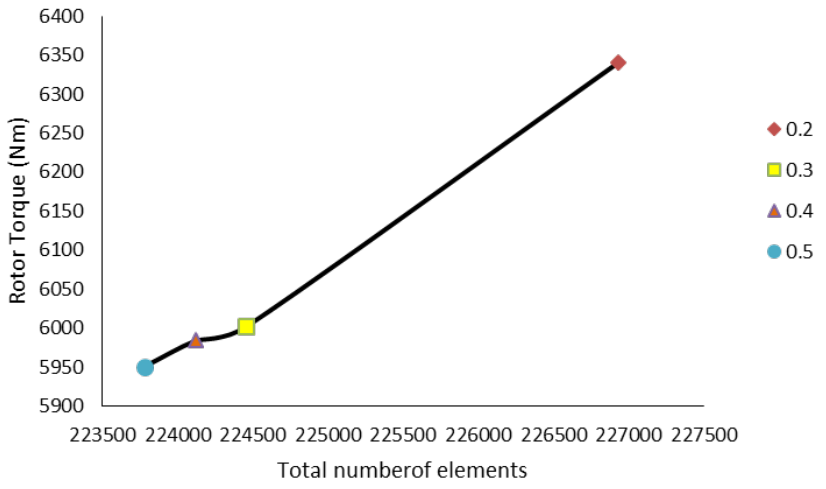


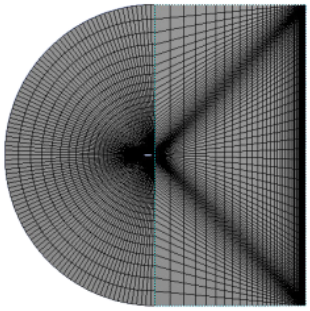

Table 2 Mesh Sensitivity

| Parameter | Mesh size at the blade surface | Mesh size at the blade surface | Mesh size at the blade surface | Mesh size |
|---|---|---|---|---|
| | 0.5 m | 0.4 m | 0.3 m | 0.2 m |
| Torque (Nm) | 5950.713 | 5984.008 | 6002 | 6340 |
| elements | 223779 | 224121 | 224457 | 226932 |

**Turbulence model**

The turbulence model utilized for this investigation is thek ω SST(shear-stress transport) model. It is a two-equation model and is created by [30], has the advantage of having the option to change from a k-ε turbulence model [31] to a k-ω turbulence model [32]. This model has been used widely in the area involving wind turbine blades with well-disposed results [33, 34]. However, to use this transport equation for the SST model to calculate the turbulent kinetic energy $k$ and the specific dissipation rate $\omega$Fluent [22] is used to analyze turbulence modeling.

**Solution method**

This paper depicts the figuring of the numerical arrangement by utilizing the ANSYS and sets out the verification of the numerical outcomes. The air is considered as incompressible [35]. Because of this, the fluid density has been taken as 1.225 kg/m3. The viscosity is likewise thought to be consistent at 1.7894×103 kg/ms. The incompressible RANS (Reynolds-Averaged Navier-Stokes) conditions are measured utilizing the pressure-based coupled algorithm, which understands the pressure and momentum-based continuity equation in a firmly coupled way and solves it.

**Convergence criteria**

To assess the convergence for the solution of the CFD, the residual plays a vital role in acquiring it. In this study, six variables of residual values are monitored during the calculation process and they are continuity, x velocity, y velocity, z velocity, turbulent kinetic energy $k$ and the specific dissipation rate $\omega$. The solution is deemed to be converged when these residual values below $10^4$ [36] which is the typical value used for residual convergence criterion in the CFD modeling of wind turbine blades. An example of a history of residual values is depicted in Figure 12. In this case, the wind speed, rotor rotational speed, pitch angle are 7m/s, 72rpm, 5° respectively. As can be seen from Figure 12, the residual values of all variables are less than $10^4$, meeting the convergence criterion.

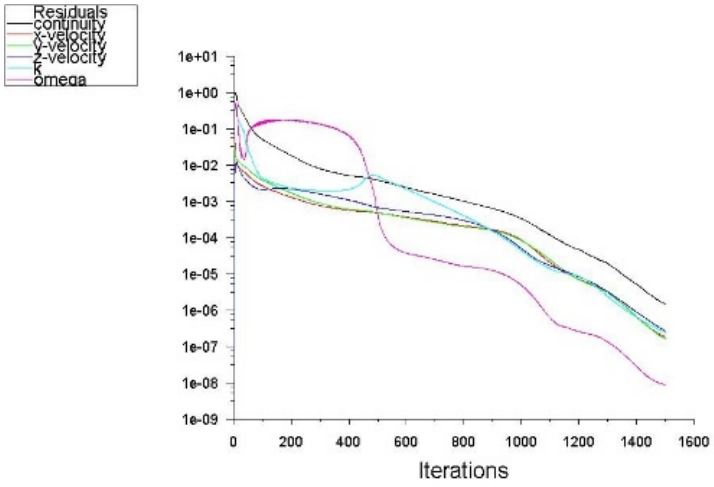




# RESULTS AND DISCUSSIONS

In this section, results from ANSYS simulations of the eight operating speeds are manifested. First, the results are displayed in the form of validation and verification performed in 2D; it is then followed by a detailed analysis of the 3d simulation of the blade. Herein, simulation has been accomplished by considering the $120^0$ sector of the turbine rotor.

## 2d simulation of flow around S809 airfoil

S809 airfoil has been selected as an airfoil from the NREL phase VI Blade to benchmark the numerical framework. The simulations are accomplished under the static condition at the velocity of 3.65 m/s, 7.30 m/s, 14.60 m/s,21.91m/s and multiple angles of attack. The pressure and velocity contour of S809 airfoil are shown in figure 13. It demonstrates that as the airflow above and below the surface of an airfoil, the formation of a starting vortex behind the airfoil near the wake expansion zone is initiated. This starting vortex rotates in a counter-clockwise direction and to maintain the conservation of angular momentum, another motion opposite to the motion of starting vortex needs to be generated, which further leads to the formation of circulation around the airfoil. The velocity vector that formed due to circulation adds to the free stream velocity vectors, thus resulting in a higher velocity above the airfoil and lower velocity below the airfoil. Considering this variation and implementing Bernoulli's equations, the pressure difference can be opted out from the surfaces of the airfoil. Due to the pressure differences, there is higher pressure at the lower surface of the airfoil and lower pressure at the upper surface of the airfoil and this eventually leads to the generation of the lift.

In figure 13, every color tone has some meaningful significance. Here red color tone signifies maximum value, whereas dark value signifies the least. Green color and yellow tone maintain the optimized range. Here in figure 13, the upper part portrays velocity contour and the lower one reflects pressure contour. In the velocity contour, at the leading edge of the airfoil and velocity near to the surface of the airfoil is very less due to stagnation point and due to this, colour tone here is blue which is reflecting less value. When moving slowly away from the airfoil surface the colour tone also changes gradually until it reaches 0.99 free stream velocity (boundary layer thickness zone).

Figure 14 through figure 19, illustrates the validation of numerical aerodynamic results against the experimental benchmark data. The results of aerodynamic coefficients from CFD portrayed in good agreement with the benchmark data. In figure 14 and figure 15 plotting of coefficient of lift and drag obtained from numerical simulations is highlighted. In figure 16 and figure 18, both experimental results Show discrepant at AOA>=$15^0$. An error of 3% to 6% between CFD and experimental results comes when performed at Reynolds's number 1E6 at AOA<$17^0$ shown in figure 16 and figure 18. However, when the angle of attack increases, the drag coefficient of the DUT experiment [37] shows inconsistent behaviour, whereas OSU experimental results [38] especially lift and pressure drag, become more reasonable. Moreover, in figure 17 and figure 19, numerical results obtained from CFD calculation are in good agreement with CSU Experimental results [39] performed at Reynolds number $5 \times 10^5$.An average error of less than 6% comes after comparing the results.

In general, a close agreement demonstrates the correct design strategy and the appropriate choice of the boundary condition on the domain. The estimation of Aerodynamic coefficients should be reliable as it is directly related to the contribution of torque in generating lift produced

From the blade. The trend of lift coefficient is such that it first increases with an increase in the angle of attack, reach maximum up to stall angle, and after that, it starts to drop again. It displays the exact position of stall around the airfoil and demonstrates the accuracy of the numerical setup.

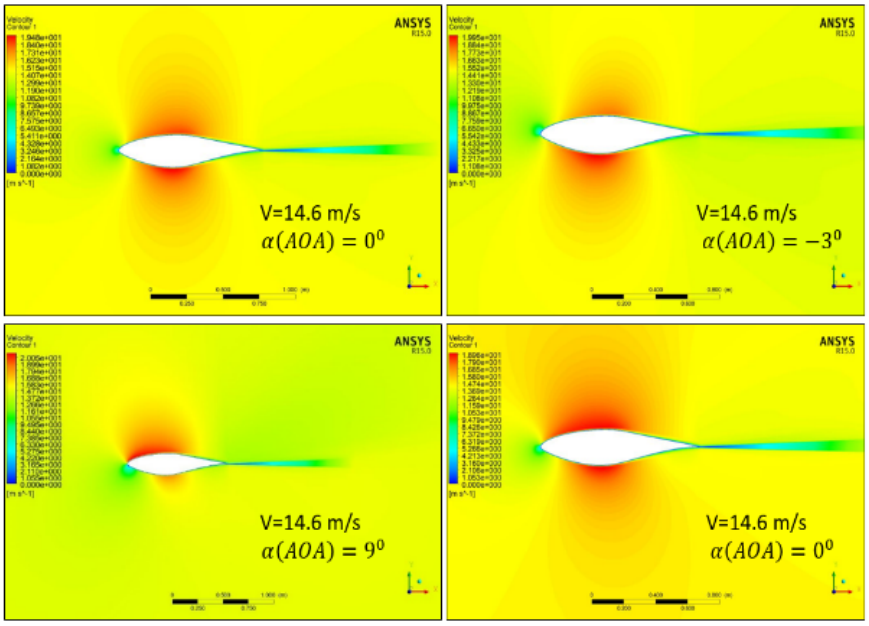

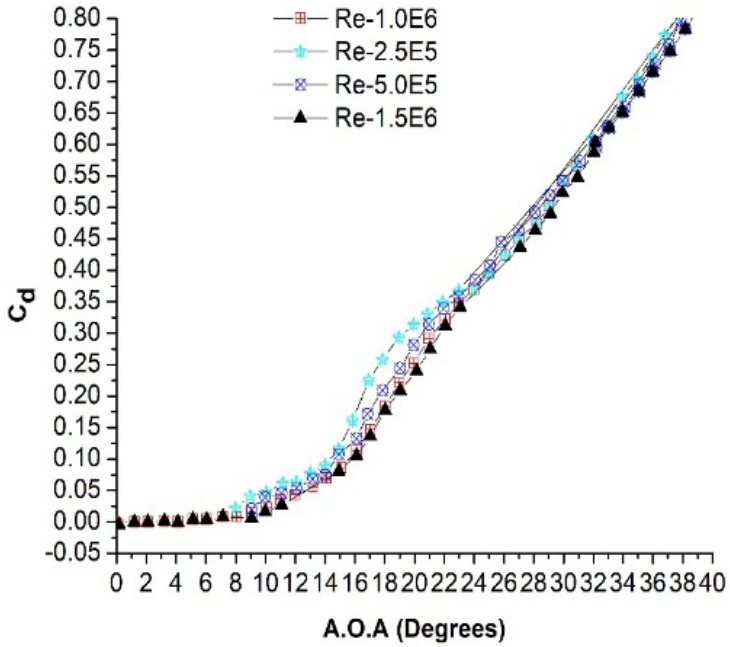


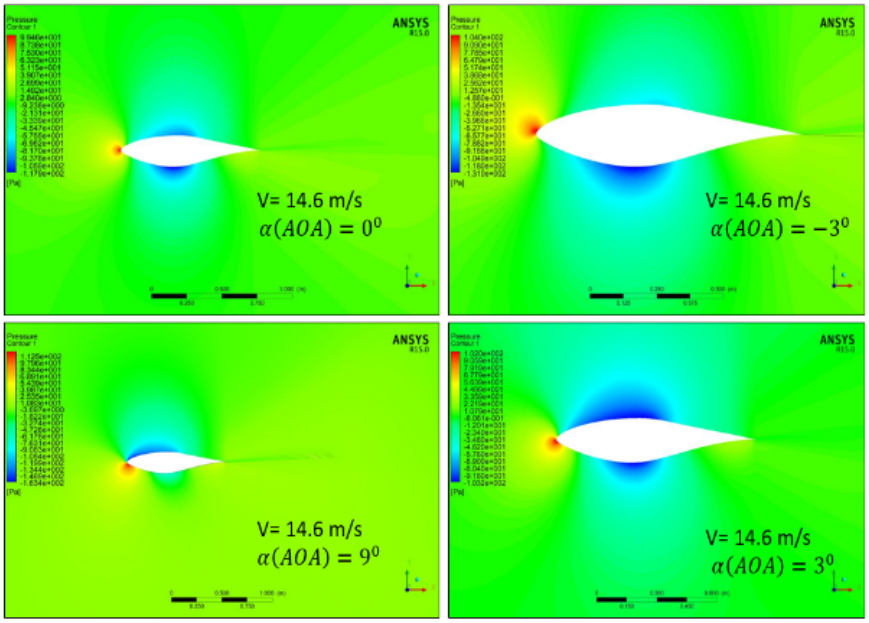

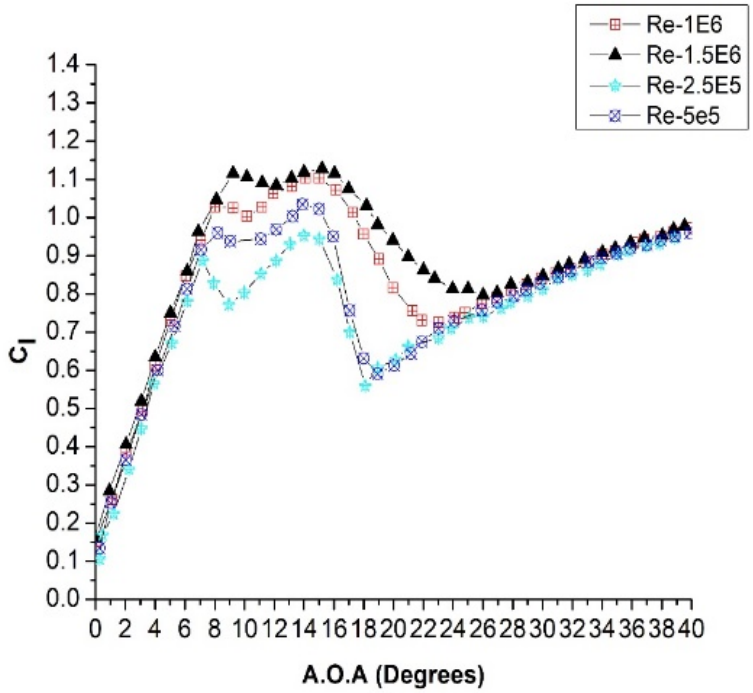


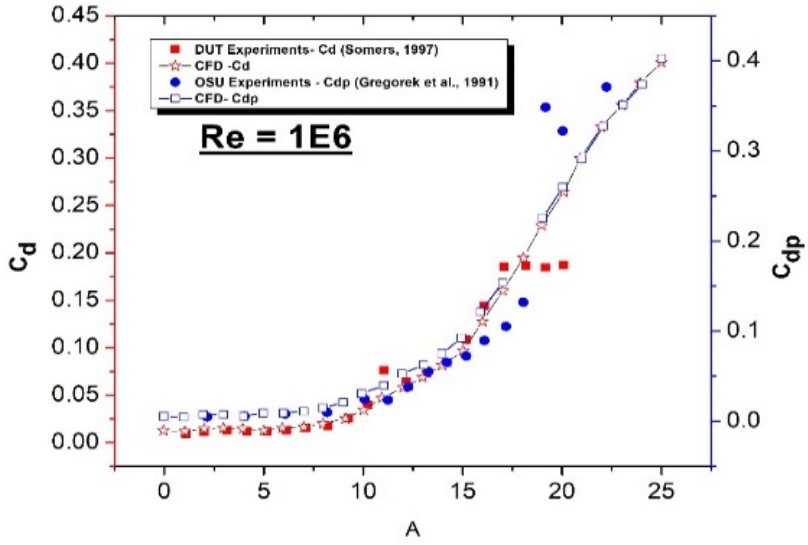

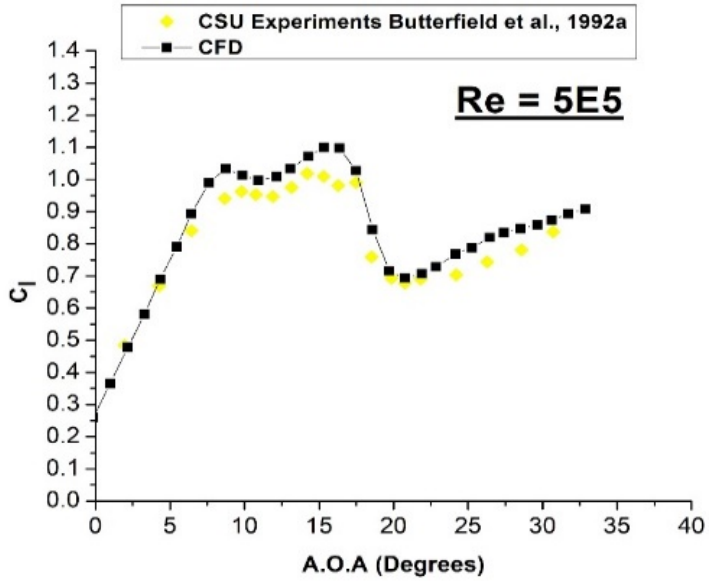


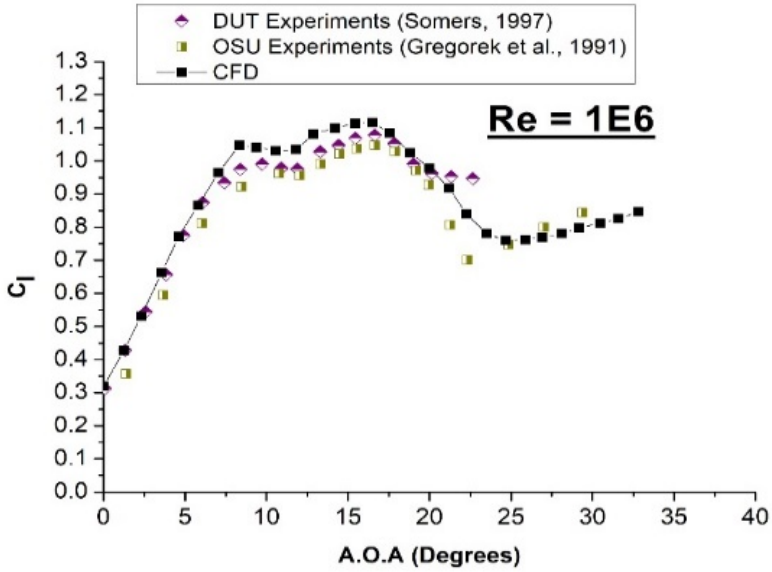

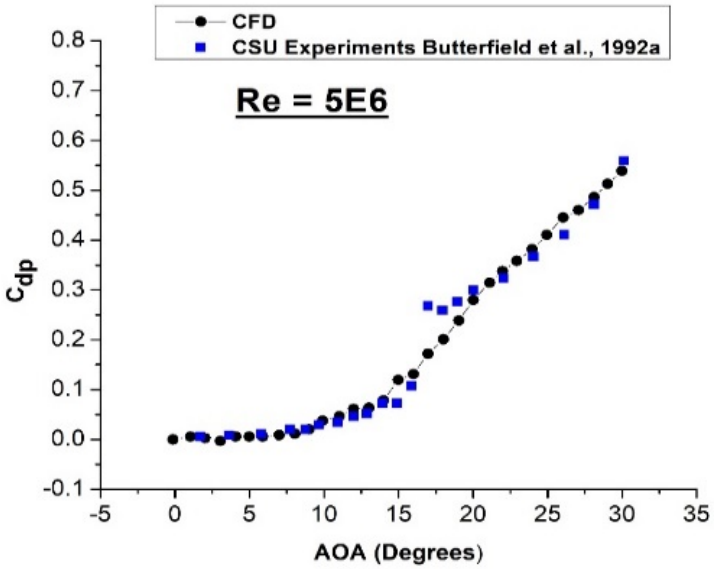


## Three-dimensional simulations

Wind-turbine blades are intended for generating power by harnessing kinetic energy through rotational effect, in which blades have variation in thickness from root to tip, allowing the blade to withstand higher stress and moment close to the root than that towards the tip. Similarly, twist to the blade is given along the span of the blade to get the maximum power coefficient. Presently, the optimization of the geometric parameters works productively in operational conditions when the turbine is rotating. However, when the turbine is not rotating, particularly in a situation when yaw and pitch control mechanism is disconnected or during a turbine-erection stage, the optimized blade twist will make the stream 3D misleadingly contrasted with the genuine rotor stream itself. Subsequently, During the shutdown, without a wind turbine control system, the $\alpha$ of the flow on the blade is dictated by the free wind direction, and the wind turbine may work outside the restricted operational range. In such stationary circumstances, complex 3D impacts may exist attributable to both the working conditions and the 3D complex turbine geometry. Thus, 2D simulation performed in the above section is sufficiently bad to comprehend flow dynamics in such conditions. It presently features the significance of performing stationary simulations which can represent the effect of bluffness of the turbine geometry and evolving cross-segment on optimal design parameters and flow physics. Therefore, this section provides the results of 3d simulation by considering stationary NREL PHASE VI wind turbine blade for analysis.

Figure 20 to figure 23 is highlighting the effect of pitch angles on various performance parameters like torque, power, and power coefficient. Each parameter has its own degree of significance in determining wind turbine reliability. Because of the wind turbine physics, for any wind speed, there is a most extreme power, and the power coefficient that happens when the blade pitch angle set at a specific value and free stream velocity strikes the span of the blade at a certain angle. Hence, in this study, seven-pitch angles $-5^0$, $10^0$, $-10^0$, $10^0$, $20^0$,$30^0$ and $40^0$ have been considered, to decide the wind speed at which the power output of the wind turbine to reach its greatest. Figure 20 illustrated the variation of torque with different wind speeds at different pitch angles. Herein, Torque increases with an increase in wind speed until the blade occupied a certain pitch angle where value drops down. The complete simulation is performed in multiple reference frames. Blade exhibiting pitch angle of $-5^0$, $10^0$, $-10^0$, $10^0$shown rise in torque value, but when the blade has given pitch angle of $20^0$,$30^0$ and $40^0$,the graph shows a different trend. Torque is an important parameter in determining the power of wind turbine blade and figure 20 is giving an idea that pitch angle has some

impactful presence in getting torque and ascertaining wind turbine efficiency for free stream velocity. It is thus become important to see the impact of pitch angle on the performance parameter of the wind turbine blade. The variation in trend in the figure 20 is such that, there is an increase of 0.53% in the value of torque when wind velocity changes from 5 m/s to 7 m/s, but, it shows some significant decrease in torque value when velocity of the flow is 13 m/s, 15 m/s, 15.1 m/s and 20 m/s. However, there is a 2% increase in torque value when velocity changes from 20 m/s to 25 m/s and 25.1 m/s. Now, for pitch 30 and pitch 40 as the free stream velocity increases torque decreases accordingly. Figure 24 to figure 26, variation of angle of attack along the span of the blade and is calculated according to the method described in [40] and [41]. The detailed estimated data of performance parameters are given in table 3, table4, table5, table 6.

Table 3 Estimation of torque for different pitch angle and wind speed using CFD

| Pitch angle (degree) | $5^0$ | $-5^0$ | $10^0$ | $-10^0$ | $20^0$ | $30^0$ | $40^0$ |
|---|---|---|---|---|---|---|---|
| velocity | Power (Watt) | Power (Watt) | Power (Watt) | Power (Watt) | Power (Watt) | Power (Watt) | Power (Watt) |
| 5 | 44587.92 | 48855.46 | 41556.98 | 48876.12 | 35242.9 | 27874.75 | 21306.65 |
| 7 | 45254.06 | 49679.19 | 42241.82 | 49805.93 | 35429.81 | 27449.88 | 21096.14 |
| 10 | 46447.16 | 50903.88 | 42390.66 | 50762.66 | 34820.97 | 26807.19 | 19965.17 |
| 13 | 51664.35 | 51664.35 | 42204.65 | 52425.49 | 33929.01 | 26581.75 | 19945.41 |
| 15 | 46815.26 | 52170.5 | 41984.11 | 53621.24 | 33299.73 | 26036.62 | 19856.44 |
| 15.1 | 46764.44 | 52360.05 | 41983.21 | 53591.68 | 33298.3 | 26019.5 | 19843.1 |
| 20 | 48295.78 | 54768.27 | 43014.35 | 57362.57 | 32788.53 | 25350.42 | 16668.75 |
| 25 | 50949.65 | 57273.76 | 44761.63 | 61467.33 | 33661.57 | 24244.32 | 11043.66 |
| 25.1 | 51000.62 | 57347.8 | 44805.97 | 61573.34 | 33467.12 | 24187.1 | 10894.45 |

Table 4 Estimation of power for different pitch angle and wind speed

| Pitch angle (degree) | $5^0$ | $-5^0$ | $10^0$ | $-10^0$ | $20^0$ | $30^0$ | $40^0$ |
|---|---|---|---|---|---|---|---|
| velocity | Power (Watt) | Power (Watt) | Power (Watt) | Power (Watt) | Power (Watt) | Power (Watt) | Power (Watt) |
| 5 | 44587.92 | 48855.46 | 41556.98 | 48876.12 | 35242.9 | 27874.75 | 21306.65 |
| 7 | 45254.06 | 49679.19 | 42241.82 | 49805.93 | 35429.81 | 27449.88 | 21096.14 |
| 10 | 46447.16 | 50903.88 | 42390.66 | 50762.66 | 34820.97 | 26807.19 | 19965.17 |
| 13 | 51664.35 | 51664.35 | 42204.65 | 52425.49 | 33929.01 | 26581.75 | 19945.41 |
| 15 | 46815.26 | 52170.5 | 41984.11 | 53621.24 | 33299.73 | 26036.62 | 19856.44 |
| 15.1 | 46764.44 | 52360.05 | 41983.21 | 53591.68 | 33298.3 | 26019.5 | 19843.1 |
| 20 | 48295.78 | 54768.27 | 43014.35 | 57362.57 | 32788.53 | 25350.42 | 16668.75 |
| 25 | 50949.65 | 57273.76 | 44761.63 | 61467.33 | 33661.57 | 24244.32 | 11043.66 |
| 25.1 | 51000.62 | 57347.8 | 44805.97 | 61573.34 | 33467.12 | 24187.1 | 10894.45 |

Table 5 Estimation of power coefficient for different pitch angle and Tip speed ratio

| Pitch angle | $5^0$ | $-5^0$ | $10^0$ | $-10^0$ | $20^0$ | $30^0$ | $40^0$ |
|---|---|---|---|---|---|---|---|
| Tip speed ratio | Torque | Torque | Torque | Torque | Torque | Torque | Torque |
| 8.342068 | 5913.65 | 6479.65 | 5511.66 | 6482.39 | 4674.23 | 3697 | 2825.88 |
| 5.95862 | 6002 | 6588.9 | 5602.49 | 6605.71 | 4699.02 | 3640.65 | 2797.96 |
| 4.171034 | 6160.24 | 6751.33 | 5622.23 | 6732.6 | 4618.27 | 3555.41 | 2647.96 |

| Pitch angle | $5^0$ | $-5^0$ | $10^0$ | $-10^0$ | $20^0$ | $30^0$ | $40^0$ |
|---|---|---|---|---|---|---|---|
| 3.208488 | 6852.19 | 6852.19 | 5597.56 | 6953.14 | 4499.97 | 3525.51 | 2645.34 |
| 2.780689 | 6209.06 | 6919.32 | 5568.31 | 7111.73 | 4416.51 | 3453.21 | 2633.54 |
| 2.762274 | 6202.32 | 6944.46 | 5568.19 | 7107.81 | 4416.32 | 3450.94 | 2631.77 |
| 2.085517 | 6405.42 | 7263.86 | 5704.95 | 7607.94 | 4348.71 | 3362.2 | 2210.76 |
| 1.668414 | 6757.4 | 7596.16 | 5936.69 | 8152.35 | 4464.5 | 3215.5 | 1464.71 |
| 1.661767 | 6764.16 | 7605.98 | 5942.57 | 8166.41 | 4438.71 | 3207.91 | 1444.92 |

Table 6 Estimation of torque for different pitch angle and tip speed ratio

| Pitch angle | $5^0$ | $-5^0$ | $10^0$ | $-10^0$ | $20^0$ | $30^0$ | $40^0$ |
|---|---|---|---|---|---|---|---|
| Tip speed ratio | Torque | Torque | Torque | Torque | Torque | Torque | Torque |
| 8.342068 | 5913.65 | 6479.65 | 5511.66 | 6482.39 | 4674.23 | 3697 | 2825.88 |
| 5.95862 | 6002 | 6588.9 | 5602.49 | 6605.71 | 4699.02 | 3640.65 | 2797.96 |
| 4.171034 | 6160.24 | 6751.33 | 5622.23 | 6732.6 | 4618.27 | 3555.41 | 2647.96 |
| 3.208488 | 6852.19 | 6852.19 | 5597.56 | 6953.14 | 4499.97 | 3525.51 | 2645.34 |
| 2.780689 | 6209.06 | 6919.32 | 5568.31 | 7111.73 | 4416.51 | 3453.21 | 2633.54 |
| 2.762274 | 6202.32 | 6944.46 | 5568.19 | 7107.81 | 4416.32 | 3450.94 | 2631.77 |
| 2.085517 | 6405.42 | 7263.86 | 5704.95 | 7607.94 | 4348.71 | 3362.2 | 2210.76 |
| 1.668414 | 6757.4 | 7596.16 | 5936.69 | 8152.35 | 4464.5 | 3215.5 | 1464.71 |
| 1.661767 | 6764.16 | 7605.98 | 5942.57 | 8166.41 | 4438.71 | 3207.91 | 1444.92 |

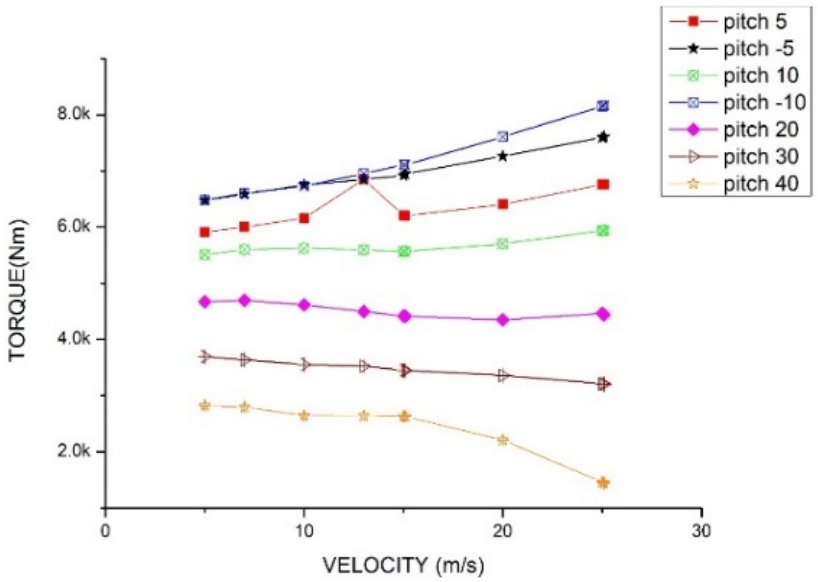

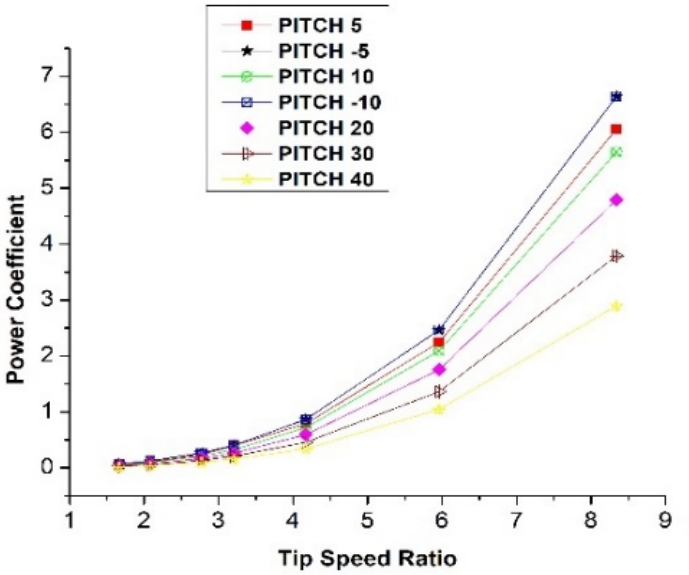


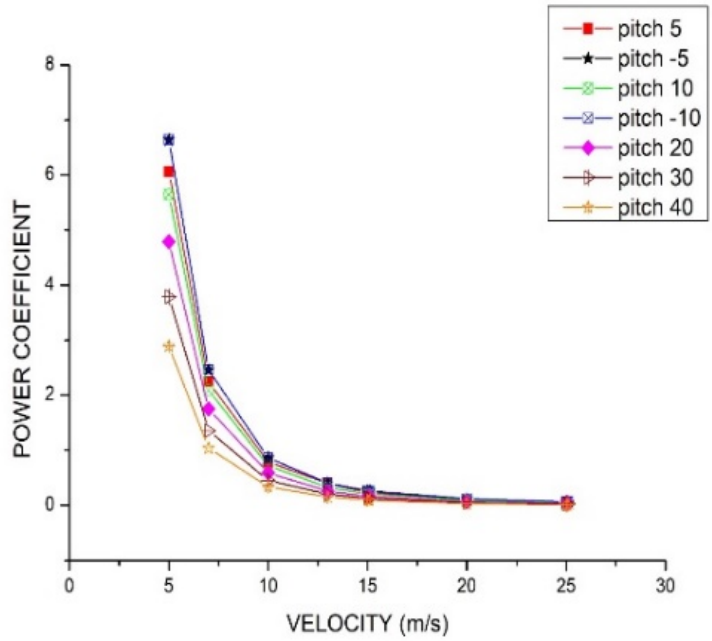

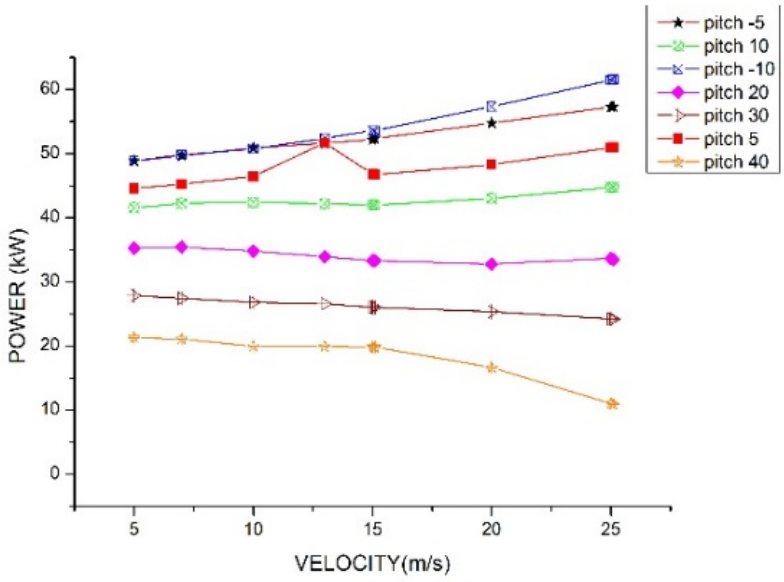


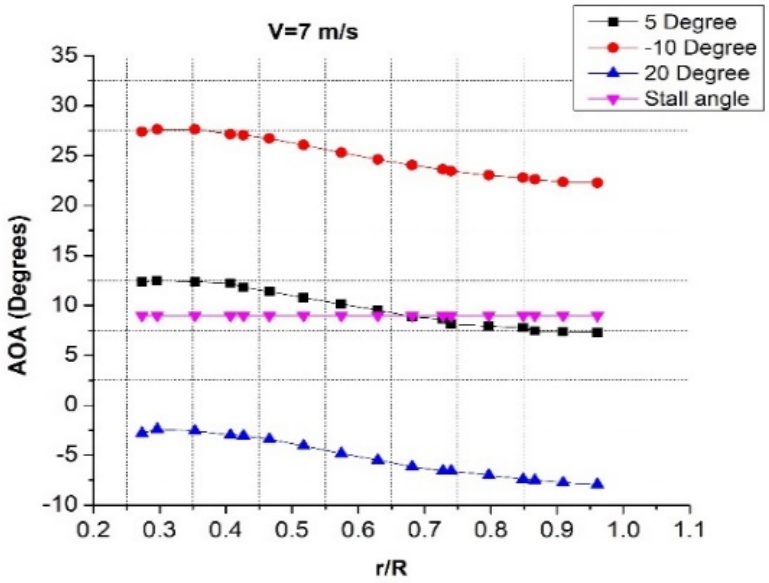

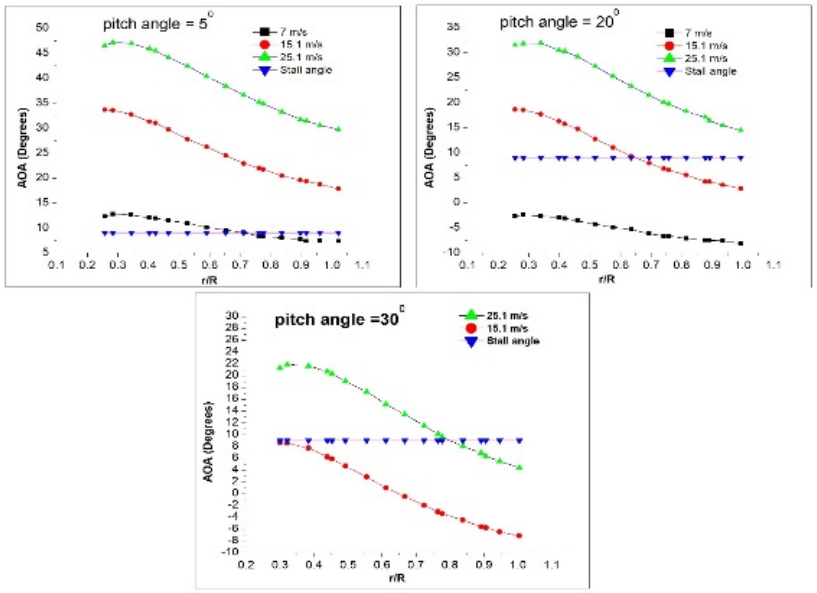


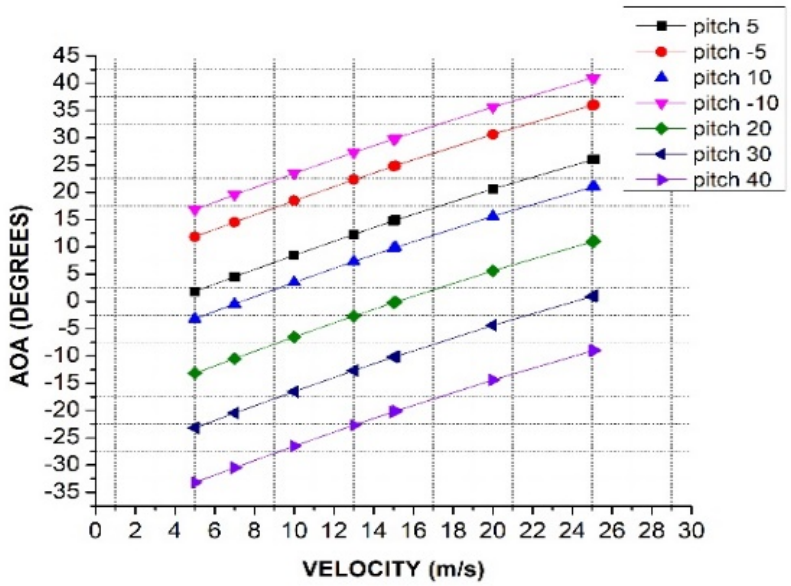


**Pressure distributions**

Figure 27 to figure 31 shows the wind pressure distributions on the blade surface obtained through a CFD analysis, and it is in the form of contours. Here in the pressure contours, the maximum pressure obtained is closer to the tip and less at the section near the hub. For each velocity and pitch angles, pressure contours on both top surface (pressure) and bottom surface (suction) of the blade are produced. As can be seen from the figure, the negative pressure is observed at the edge of the bottom surface (suction side), and the positive pressure observed at the edge of top surface (pressure side).however as the pitch angle of the blade changes, the position of blade shows some deviation with the airflow which further cause stagnation point

to change its position and move towards the suction side and results with negative pressure on the opposite side of the bladed due to reducing air velocity. Now, in this section, the Distribution of pressure is justified following the three-stall region. One is a pre-stall region that occurs before 9 m/s; second is the dynamic stall region that comes into play when wind speed is 13 m/s to 17 m/s and third is deep stall region which occurs at velocity more than 20 m/s. As can be seen from the graph that in the pre stall region (5m/s, 7 m/s), the pressure distribution shows some significant change as the pitch angle of the blade changes. When the velocity is 5 m/s, the trend of maximum pressure decreases exponentially from 753.7 Pascal at $-10^0$pitch angle to 400 Pascal at $40^0$ pitch angle. However, the trend of minimum pressure shows some up and down variation, such as at $-10^0$ the highest negative pressure is -1000 Pascal followed by -811.7 Pascal for $10^0$ pitch angle which further shows some variation by changing the pressure to -938.4 Pascal for $20^0$degree pitch angle and subsequently ended to -951.9 Pascal and -865.8 Pascal for the pitch angle $30^0$ and $40^0$. Now for 7 m/s, the trend of maximum pressure shows the same variation as obtained from 5 m/s but for minimum pressure, the pattern is such that it first decreases from -1417 Pascal at $-10^0$ pitch angle to -811.7 Pascal at $10^0$ pitch angle and then increases as it progresses the pitch angle from $20^0$ to $40^0$ in step of $10^0$. The position of maximum pressure occurs at the center position near to the tip. The variation of color tone is symmetric on both sides of the maximum pressure location. Here in the contour diagram, the red color tone indicates maximum pressure and dark blue reflects minimum pressure. Whereas, yellow and green color tones are displaying the average pressure range which can be seen at the maximum place over the surface, may it be top surface or bottom surface. In the deep-stall region, for the pitch angles $10^0$ and $-10^0$, the pressure distribution of the blade is nearly similar when the wind velocity is 20 m/s and 25 m/s. however, the distribution of maximum pressure and minimum pressure over the top surface of the blade shows some discrepancy when the wind velocity reaches 25.1 m/s. the distributions are such that the bottom surface is no more dominated with blue color tone(highest negative pressure) as seen in the pre-stall region and also when the velocity is 20 m/s and 25 m/s for a deep stall region. The top surface in the other hand also shows some deviation in the smoothness of the red color tone (highest positive pressure) and is overshadowed by green color one near the root. Now, when pitch angle of $20^0$, $30^0$, $40^0$ was taken and deep stall velocities are considered for the analysis, the pressure distributions show high deviation from the pre-stall one. With an increase in pitch angle, all deep stall velocities possess variation in pressure distribution.

Moreover, in the deep-stall region, the effects of the leading-edge suction become insignificant, and strong suction occurs at the isolated small area of the leading edge near the hub, which has little influence on the aerodynamic force. Here, a greater differential of the pressure distribution on the blade surface is mainly due to the three-dimensional rotation effect and flow separation on the blade. As can be seen from the graph above, the position that is closer to the root of blade exhibit larger angle of attack, which results in stalling of airfoil and flow separation, which further leads to Separation of the vortex at trailing edge and thus create a pressure distribution on the surface of the blade and induced a violent pressure fluctuation will be induced. Because of this, pressure distribution shown in figure 27 to figure 31 exerts irregular in color band, especially near the trailing edge. A greater differential is shown at the leading edge than the trailing edge, especially near the tip of the blade. There is a low-pressure area at the tip of the blade on the pressure surface of the blade. It is mainly caused by three-

Dimensional rotation effect at the tip of the blade. In this area, part of the air flows from the pressure surface to suction surface through the tip of the blade

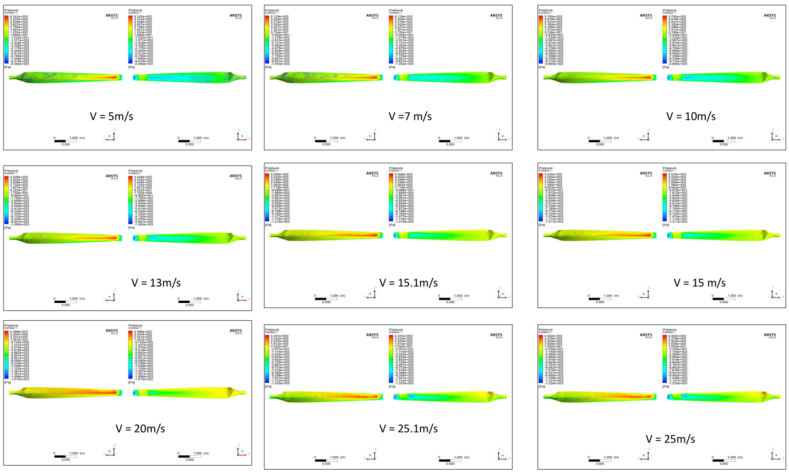


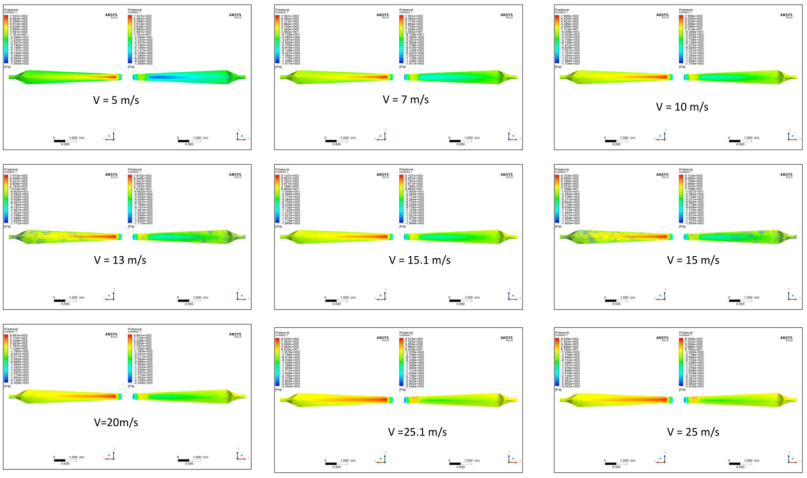

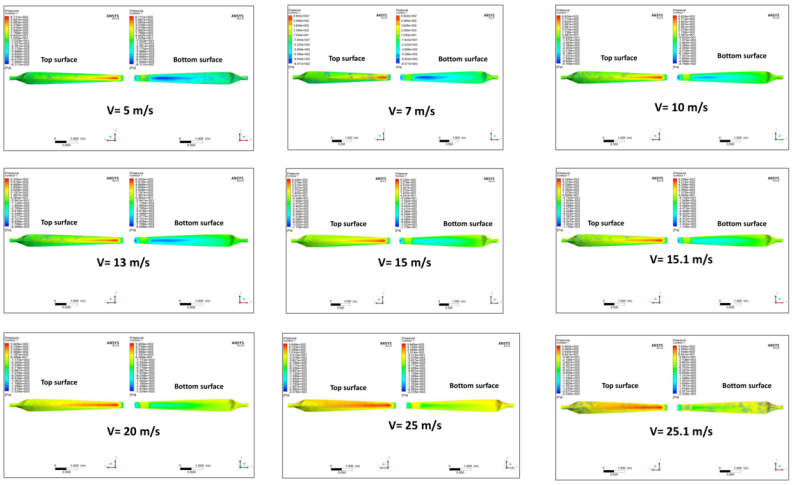


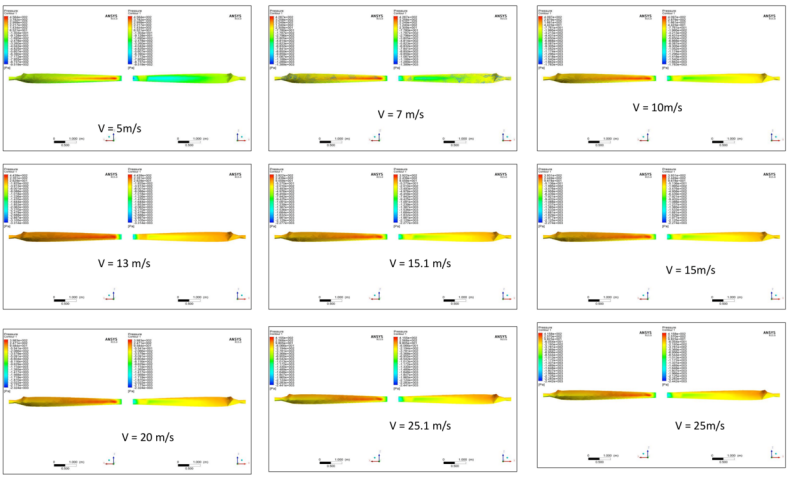


# CONCLUSIONS

In this study, the effect of blade pitch angle on the aerodynamic characteristics of the HAWT was investigated via CFD simulations, and the conclusions can be summarized as follows

- Numerical investigation of S809 airfoil shows that the aerodynamic coefficients from the present model provide reasonable agreement with the results from benchmark data
- There is the highest positive pressure when the blade pitch angle is -$10^0$ and velocity is 25.1 m/s, and the lowest positive pressure when the blade pitch angle is $40^0$and velocity is 20 m/s. however, When the blade pitch angle is $30^0$ and velocity is 13 m/s, the blade exhibits the highest negative pressure and when the blade pitch angle is $10^0$ and velocity is 5 m/s blade possess lowest negative pressure.
- The torque acting on the blade is maximum when the pitch angle is -$10^0$ and minimum when the blade pitch angle is $40^0$. However, in both the case the wind velocity is 25.1 m/s.
- When the velocity of the flow is 5m/s and 7 m/s, the effect of pitch angles over predicted the limit of power coefficient which is not possible in a real application, however, when the wind velocity changes

to 10 m/s, 13 m/s,15 m/s and 15.1 m/s, the results of power coefficient approaches closer to the real value (0.3-0.4). However, when velocity increases to 20 m/s, 25 m/s and 25.1 m/s, the results of power coefficients are below par the real value. The conclusion can be derived from the above that, In addition to the effect of pitch angle, velocity is also playing a vital role in determining the effective power coefficient.


## ACKNOWLEDGEMENTS


## Disclosure

**Conflict of interest:** Authors declare that they have no conflict of interest

## REFERENCES


1. Yilmaz, A. S., & Özer, Z. (2009). Pitch angle control in wind turbines above the rated wind speed by multi-layer perceptron and radial basis function neural networks. *Expert Systems with Applications* , *36* (6), 9767-9775.
2. Grieser, B., Sunak, Y., & Madlener, R. (2015). Economics of small wind turbines in urban settings: An empirical investigation for Germany. *Renewable Energy* , *78* , 334-350.
3. Abdelkafi, A., & Krichen, L. (2011). New strategy of pitch angle control for energy management of a wind farm. *Energy* , *36* (3), 1470-1479.
4. Slootweg, J. G., De Haan, S. W. H., Polinder, H., & Kling, W. L. (2003). General model for representing variable speed wind turbines in power system dynamics simulations. *IEEE Transactions on power systems* , *18* (1), 144-151.
5. Fraile, A. Mbistrova, Wind in power: 2017 European statistics. The European Wind Association. (2018) 3 – 25.
6. Bahaj, A. S., Myers, L., & James, P. A. B. (2007). Urban energy generation: Influence of micro-wind turbine output on electricity consumption in buildings. *Energy and buildings* , *39* (2), 154-165.
7. Miller, W Chang, R. Issa, G. Chen, Review of computer-aided numerical simulation in wind energy, Renew. Sustain. Energy Rev. 25 (2013) 122—134.
8. R. Lanzafame, M. Messina, Horizontal axis wind turbine working at maximum power coefficient continuously, Renew. Energy 35 (2010) 301—306.
9. J.C. Dai, Y.P. Hu, D.S. Liu, X. Long, Aerodynamic loads calculation and analysis for large scale wind turbine based on combining REM modified theory with dynamic stall model, Renew, Energy 36(2011) 1095—1104.
10. J.R.P. Vaz, J.T. Pinho, A.L Amarante Mesquita, An extension of BEM method applied lo horizontal-axis wind turbine design, Renew. Energy 36 (2011)1734—1 740.
11. E.P.N. Duque, C.P. van Darn, S.C Hughes, Navier stokes simulations of the NREL Combined experiment phase II rotor, AIAA-99-0037, 1999, pp. 143—153.
12. G. Xu, LN. Sankar, Computational study of horizontal axis wind turbines, J. Sol.Energy Eng. 122(2000) 35—39.
13. G. Xu, LN. Sankar, Application of a viscous flow methodology to the NREL phase VI rotor, AIAA-2002-0030, 2002, pp. 84-93.
14. J. Johansen, N.N. Sorensen,J.A. Michelsen, S. Schreck, Detached-Eddy simulation of flow around the NREL phase Vi blade, AIAA-2002-0032, 2002, pp. 106-114.
15. E.P.N, Duque, M.D. Iurklund, W, Johnson, Navier-Stokes and comprehensive analysis performance predictions of the NREL phase VI experiment, AIAA-2003-0355, 2003, pp. 1—19.
16. N. Sezer-Uzol, LN. L.ong, 3-D time-accurate CFD simulations of wind turbine rotor flow fields, AIAA-2006-394, 2006, pp. 1 —23.
17. Thumthae, T. Chitsomboon, Optimal angle of attack [or untwisted blade wind turbine, Renew. Energy 34 (2009) 1279—1284.
18. J.-O. Mo, Y.-H.Lee, CFD Investigation on the aerodynamic characteristics of a small-sized wind turbine of NREL PHASE VI operating with a stall-regulated method, J. Mech. Sci. Technol. 26(1) (2012) 81—92.

19. Y. li, K.-J. Paik, T. Xing, P.M. Carrica, dynamic overset CFD simulations of wind turbine aerodynamics, Renew. Energy 37 (2012) 285—298.
20. John, D. and J. Anderson, *Computational fluid dynamics: the basics with applications.* P. Perback,633 International ed., Published, 1995
21. MM. Hand, D.A. Simms, L.J. Fingersh, D.W. Jager, J.R. Correll, S. Schreck,cl al., Unsteady aerodynamics, experiment phase VI: wind tunnel test configurations and available data campaigns. Technical Report NREL JTP-500-29955, 2001.
22. Fluent, A. N. S. Y. S. (2016). Fluent 15 users guide. *Lebanon, USA* .
23. Langtry, R., Gola, J., & Menter, F. (2006, January). Predicting 2D airfoil and 3D wind turbine rotor performance using a transition model for general CFD codes. In *44th AIAA aerospace sciences meeting and exhibit* (p. 395).
24. Klausmeyer, S. M., & Lin, J. C. (1997). Comparative results from a CFD challenge over a 2D three-element high-lift airfoil.
25. Kim, B. S., Kim, M. E., & Lee, Y. H. (2008). Predicting the aerodynamic characteristics of 2D airfoil and the performance of 3D wind turbine using a CFD code. *Transactions of the Korean Society of Mechanical Engineers B* , *32* (7), 549-557.
26. Sørensen, N. N. (2009). CFD modelling of laminar-turbulent transition for airfoils and rotors using the γ- model. *Wind Energy: An International Journal for Progress and Applications in Wind Power Conversion Technology* , *12* (8), 715-733.
27. Roul, R., Kumar, A., & Mohanty, S. C. (2019, May). Numerical Investigation of Fluid Structure Interaction of 1.5 MW Wind Turbine Rotor Blade System. In *Proceedings of the 2019 International Conference on Management Science and Industrial Engineering* (pp. 254-259).
28. Wang, L., Quant, R., & Kolios, A. (2016). Fluid structure interaction modelling of horizontal-axis wind turbine blades based on CFD and FEA. *Journal of Wind Engineering and Industrial Aerodynamics* , *158* , 11-25.
29. Bazilevs, Y., Hsu, M. C., & Scott, M. A. (2012). Isogeometric fluid–structure interaction analysis with emphasis on non-matching discretizations, and with application to wind turbines. *Computer Methods in Applied Mechanics and Engineering* , *249* , 28-41.
30. Menter, F. L. O. R. I. A. N. R. (1993, July). Zonal two equation kw turbulence models for aerodynamic flows. In *23rd fluid dynamics, plasma dynamics, and lasers conference* (p. 2906).
31. Jones, W. P., & Launder, B. (1972). The prediction of laminarization with a two-equation model of turbulence. *International journal of heat and mass transfer* , *15* (2), 301-314.
32. Wilcox, D. C. (2008). Formulation of the kw turbulence model revisited. *AIAA Journal* , *46* (11), 2823-2838.
33. Sørensen, N. N., Michelsen, J. A., & Schreck, S. (2002). Navier–Stokes predictions of the NREL phase VI rotor in the NASA Ames 80 ft× 120 ft wind tunnel. *Wind Energy* , *5* (2-3), 151-169.
34. Mo, J. O., & Lee, Y. H. (2012). CFD Investigation on the aerodynamic characteristics of a small-sized wind turbine of NREL PHASE VI operating with a stall-regulated method. *Journal of mechanical science and technology* , *26* (1), 81-92.
35. Anderson Jr, J.D., 2011. Fundamentals of Aerodynamics. Tata McGraw-Hill Educa- tion, New York.
36. Yelmule, M.M., Vsj, E.A., 2013.CFD predictions of NREL phase VI rotor experiments in NASA/AMES wind tunnel. Int.J.Renew.Energy Res.3, 261–269.
37. Somers. D.M., 1997. Design and Experimental Results for the S809 Airfoil. NREL/SR 440-6918.
38. Gregorek G.M., Hoffmann M.J. and Mulh KE. 3-D Wind Tunnel Tests of the S809 airfoil Model, 1991, Aeronautical and Astronautical Research Laboratory. Ohio State University.
39. Butterfield. CP., Musial, W.P., Simms, DA., 1992a. Combined Experiment Final Report—Phase II. NREL TP-422-4807.
40. Thumthae, C., & Chitsomboon, T. (2009). Optimal angle of attack for untwisted blade wind turbine. *Renewable energy* , *34* (5), 1279-1284.
41. Mo, J. O., & Lee, Y. H. (2012). CFD Investigation on the aerodynamic characteristics of a small-sized wind turbine of NREL PHASE VI operating with a stall-regulated method. *Journal of mechanical*

*science and technology* , *26* (1), 81-92.